

RAAG: RATIO AWARE ADAPTIVE GUIDANCE

Shangwen Zhu^{1*}, Qianyu Peng^{1*}, Yuting Hu¹, Zhantao Yang¹,

Han Zhang¹, Zhao Pu¹, Ruili Feng², Fan Cheng^{1†}

¹Shanghai Jiao Tong University, Shanghai, China

²University of Waterloo, Ontario, Canada



Figure 1: Superior Efficiency of RAAG: Our method achieves comparable quality to 30-step CFG image generation with only 10 steps, demonstrating a $3.0\times$ **speedup** over standard CFG sampling on Stable Diffusion v3.5.

ABSTRACT

Flow-based generative models have recently achieved remarkable progress in image and video synthesis, with classifier-free guidance (CFG) becoming the standard tool for high-fidelity, controllable generation. However, despite their practical success, little is known

*These authors contributed equally to this work.

†Corresponding author

about how guidance interacts with different stages of the sampling process—especially in the fast, low-step regimes typical of modern flow-based pipelines. In this work, we uncover and analyze a fundamental instability: the earliest reverse steps are acutely sensitive to the guidance scale, owing to a pronounced spike in the relative strength (RATIO) of conditional to unconditional predictions. Through rigorous theoretical analysis and empirical validation, we show that this RATIO spike is intrinsic to the data distribution, independent of the model architecture, and causes exponential error amplification when paired with strong guidance.

To address this, we propose a simple, theoretically grounded, RATIO-aware adaptive guidance schedule that automatically dampens the guidance scale at early steps based on the evolving RATIO, using a closed-form exponential decay. Our method is lightweight, requires no additional inference overhead, and is compatible with standard flow frameworks. Experiments across state-of-the-art image (SD3.5, Lumina) and video (WAN2.1) models demonstrate that our approach enables up to $3\times$ faster sampling while maintaining or improving generation quality, robustness, and semantic alignment. Extensive ablation studies further confirm the generality and stability of our schedule across models, datasets, and hyperparameters. Our findings highlight the critical role of stepwise guidance adaptation in unlocking the full potential of fast flow-based generative models.

1 INTRODUCTION

Over the past few years, flow-based generative models (Liu et al., 2022; Lipman et al., 2022) have rapidly advanced, offering new ways to synthesize high-quality images (Dhariwal and Nichol, 2021; Huang et al., 2024; Liang et al., 2024; Süleyman and Biricik, 2025; Xiao et al., 2024), videos (Team, 2025), and even multimodal content (Reuss et al., 2024; Ma et al., 2024; Müller-Franzes et al., 2023). Unlike score-based diffusion models that rely on a stochastic denoise-and-refine chain across hundreds of noise levels, modern flow models such as Rectified Flow (RF) learn an explicit, continuous velocity field that maps any intermediate state x_t directly toward the data manifold. Because the reverse trajectory is governed by a deterministic ODE rather than a sequence of stochastic denoising steps, it can be integrated with a high-order ODE solver in only tens of function evaluations—often an order of magnitude fewer than the hundreds required by diffusion—while simultaneously eliminating stochastic variance and preserving fidelity.

Much of this progress in both speed and controllability can be attributed to the development of classifier-free guidance (CFG) (Dhariwal and Nichol, 2021; Ho and Salimans, 2022). By blending predictions from both unconditional and conditional networks, CFG enables models to strongly follow user prompts or target labels, unlocking fine-grained control over output style, content, and meaning. As CFG has become standard, many researchers have sought to push it even further. A variety of modified guidance techniques and adaptive schedules have been proposed to better balance sample diversity, faithfulness, and quality. These approaches—*Guidance Scheduler* (Wang et al., 2024), β -CFG (Malarz et al., 2025) and *CFG-Zero** (Fan et al., 2025b)—typically focus on how to adjust the guidance strength, add constraints, or exploit extra side-information. Yet, few works have asked a more fundamental question: *how does guidance interact with the specific stages of the sampling process itself, especially in fast flow-based models?*

We uncover a previously overlooked weakness in the flow-based sampling: the very first reverse steps are strikingly sensitive to guidance. At the initial noise state the RATIO ρ —the relative magnitude of the conditional velocity to its unconditional baseline—is already $\mathcal{O}(1)$. Because standard pipelines apply a fixed guidance scale w throughout sampling, their effective control term is the *product* $w\rho$. A lower-bound analysis shows that trajectory error can grow roughly as $\exp(w\rho)$, so large $w\rho$ quickly amplifies any numerical or stochastic perturbation, producing semantic drift and visual artifacts. Conversely, reducing the RATIO—or equivalently moderating w when the RATIO is high—substantially stabilizes the early trajectory. Controlled

experiments in which we vary only the initial sampling noise confirm the prediction: lower-RATIO seeds yield markedly higher ImageReward and CLIPScore, while everything else is held constant.

To mitigate this vulnerability, we introduce a RATIO-*aware* guidance schedule. Rather than keeping w fixed for the entire trajectory, we recompute it at every reverse step via a lightweight exponential map of the current RATIO — $w(\rho_t) = 1 + (w_{\max} - 1) \exp(-\alpha \rho_t)$. This closed-form rule mirrors the trend suggested by the error-bound analysis and is further confirmed by our greedy N -step search: it retains the head-room of a large guidance scale when the conditional signal is weak ($\rho_t \approx 0$), yet rapidly attenuates guidance when the RATIO spikes. The schedule is *parameter-free at test time*, adds negligible overhead, and can be plugged into any CFG or RF pipeline without retraining.

Our adaptive guidance schedule enables substantial acceleration of conditional generation without sacrificing sample quality as measured by ImageReward, CLIPScore, and vBench. Specifically, we achieve up to $3\times$ faster inference on SD3.5 (Esser et al., 2024), $4\times$ on Lumina (Gao et al., 2024), and $2\times$ on WAN2.1-14B (Team, 2025)—each time matching or exceeding the performance of much slower baselines. Furthermore, results are robust to hyperparameter settings and generalize across model scales, datasets, and both image and video domains. As an added benefit, our approach even yields modest quality improvements in some regimes (e.g., higher imaging scores for WAN2.1-1.4B than WAN2.1-14B), further underscoring its practical effectiveness and versatility.

2 PRELIMINARY

2.1 CONDITIONAL GENERATION OPTIMIZATION

A variety of methods have aimed to improve guidance in diffusion models: **CFG++**(Chung et al., 2024) treats guidance as manifold-constrained inverse problems; **CFG Schedulers**(Xi et al.) optimizes time-dependent strength; **Apply Guidance in Interval**(Kynkäänniemi et al., 2024) restricts guidance to specific noise levels; **Adaptive Guidance**(Castillo et al., 2025) dynamically selects conditional/unconditional paths. **ReCFG**(Xia et al., 2025) corrects expectation shifts via closed-form solutions, while **TFG**(Ye et al., 2024) unifies gradient-based parameterizations. Particularly relevant, **CFG-Zero***(Fan et al., 2025b) targets flow-matching models (Esser et al., 2024; Lipman et al., 2022; Fan et al., 2025a; Liu et al., 2022; Gao et al., 2024) by compensating early-step velocity errors on SD3.5 and WAN2.1 (Team, 2025). While these methods deliver progressive improvements in controllability and detail preservation, their enhancements are often incremental and do not fundamentally address the underlying dynamics of guidance.

2.2 CLASSIFIER FREE GUIDANCE IN RECTIFIED FLOW

Consider a generative model setup where an initial data point x_0 is sampled from the data distribution p_{data} , and a final latent point x_1 is drawn from a standard normal distribution $\mathcal{N}(0, I)$. Rectified Flow (RF) defines a deterministic interpolation path between these two points via $x_t = tx_1 + (1-t)x_0$, where $t \in [0, 1]$ indexes the continuous transformation from the original data to Gaussian noise.

In this framework, the task is to predict the “velocity”—the directional and magnitude difference guiding the point x_t towards the noise point x_1 . Specifically, the unconditional velocity prediction $v_u(x_t)$ represents the expected transition direction without any conditioning information, formally defined as

$$v_u(x_t) = \mathbb{E}[x_1 - x_0 \mid x_t, \emptyset],$$

where \emptyset indicates the absence of conditioning information. The conditional velocity prediction $v_c(x_t, c)$ incorporates additional information (such as class labels or textual prompts denoted by c) to guide the transformation towards more targeted outcomes:

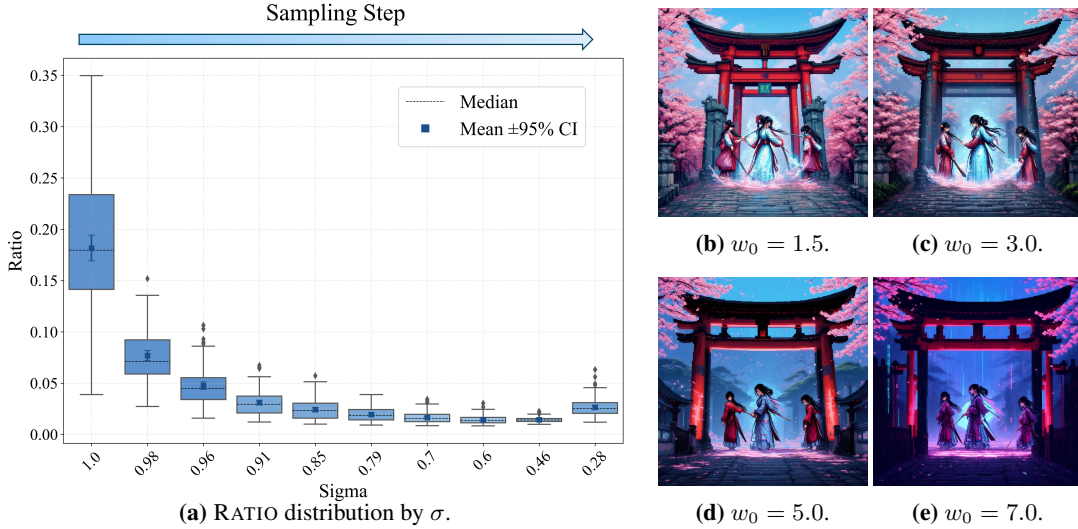


Figure 2: (a) Dynamics of the conditional-unconditional RATIO ρ during sampling. At the start of reverse sampling ($\sigma \rightarrow 1$), ρ is large—reflecting a strong relative conditional signal—but it decays swiftly over the first few steps, converging to a moderate value after certain step N . This rapid initial drop highlights the RATIO-spike phenomenon and motivates our step-adaptive guidance schedule. **(b) Effect of varying initial guidance scale w_0 on image quality in 10-step constant CFG sampling.** Only the first-step guidance scale is modified (w_0 varied), while all subsequent steps use a fixed scale of 7.0. As w_0 exceeds certain threshold, the generated images exhibit progressively worse perceptual quality, illustrating the over-steering effect of an excessively large initial guidance.

$$v_c(x_t, c) = \mathbb{E}[x_1 - x_0 \mid x_t, c].$$

CFG effectively combines these two predictions to achieve controllable and high-quality generation. The CFG formulation linearly interpolates between the unconditional and conditional velocity predictions:

$$v_{\text{cfg}}(x_t, c) = v_u(x_t) + w \cdot (v_c(x_t, c) - v_u(x_t)), \quad (1)$$

where $w > 1$ is the guidance scale controlling the strength of conditioning. A larger w strongly emphasizes the conditional information, potentially yielding more accurate but possibly less diverse generations. Conversely, smaller w values emphasize the unconditional prediction, promoting greater diversity but possibly less precise adherence to conditioning constraints.

3 RATIO AWARE ADAPTIVE GUIDANCE

Prior to formalizing our method, we introduce two central quantities that underpin our theoretical and empirical study to enable a precise analysis of how conditioning information modulates the sampling dynamics:

Definition 3.1. The *velocity gap* between conditional and unconditional velocity predictions is defined as:

$$\delta(x_t, c) = v_c(x_t, c) - v_u(x_t). \quad (2)$$

Definition 3.2. The RATIO is defined as:

$$\text{RATIO}(x_t, c) = \frac{\|\delta(x_t, c)\|_2}{\|v_u(x_t)\|_2}. \quad (3)$$

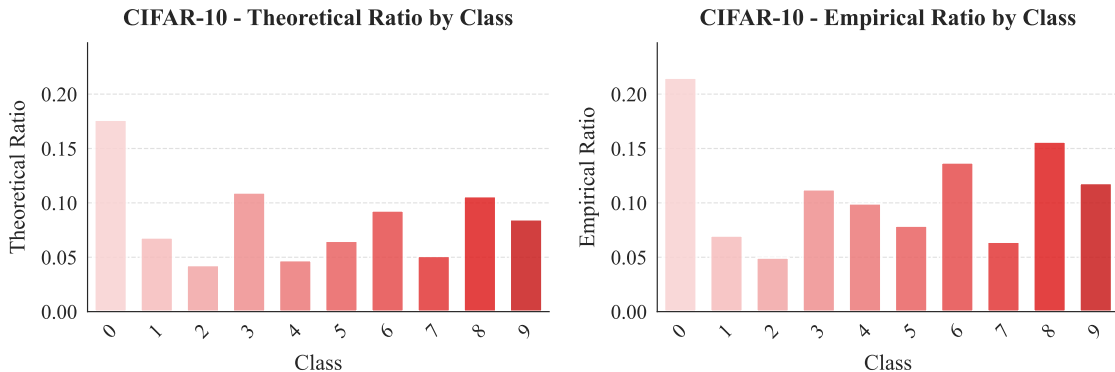


Figure 3: Agreement between theoretical and empirical first-step RATIO on CIFAR-10. Quantitative comparison between the closed-form $\rho_{t=1}$ (from $\|\mu_c - \mu_u\|_2 / \|x_1 - \mu_u\|_2$) and the empirically measured first-step RATIO across test samples, together with the corresponding RATIO distributions. The results demonstrate a high degree of consistency between theory and practice, with Pearson correlation coefficient of $r = 0.92$ on CIFAR-10.

Intuitively, Equation (3) measures the relative magnitude of the conditional signal to the unconditional "noise" prediction; a larger RATIO indicates stronger prompt influence.

Section overview. We first observe a striking sensitivity to guidance scale in early reverse steps, characterized by a sharp RATIO spike (Section 3.1). We prove this stems inherently from data distributions (Section 3.2), motivating our adaptive guidance solution for stability and quality gains (Sections 3.3 and 3.4).

3.1 EARLY-STEP GUIDANCE INSTABILITY

Disproportionate Impact of Early Guidance. We find that the guidance scale applied during the initial reverse steps exerts a disproportionate influence on the final output. As generation begins from pure noise, these first updates crucially determine the downstream semantic trajectory. Applying overly large guidance in early steps results in persistent semantic drift and artifacts, as demonstrated in Figures 2b to 2e. While previous works Sadat et al. (2024) have cautioned against excessive guidance, they have not specifically addressed the acute sensitivity of these early steps. Our results show that over-steering at this stage is especially damaging, highlighting the need for adaptive guidance strategies.

Early RATIO Spike as the Root Cause. To further probe this instability, we examine the RATIO between the conditional and unconditional velocities throughout the sampling process. Notably, we find that the RATIO exhibits a pronounced spike during the earliest reverse steps (Figure 2a), exactly when the model is most sensitive to guidance. This early surge amplifies the effect of any fixed guidance scale w , making large values especially disruptive at the start. We will theoretically discuss later why the initial RATIO tends to be large and how a large RATIO exacerbates instability during sampling, thus highlighting the necessity of RATIO-aware guidance to ensure stable generation.

3.2 ORIGIN AND INEVITABILITY OF A LARGE INITIAL RATIO

The two observations above—early-step over-steering and the accompanying RATIO spike—raise a natural question: *why is the RATIO so large at the outset?* We answer this by analyzing the RATIO of initial noise.

Definition 3.3. The unconditional data mean is defined as $\mu_u := \mathbb{E}[x_0]$, and the conditional data mean given condition c is defined as $\mu_c := \mathbb{E}[x_0 | c]$.

Here, μ_u denotes the mean of all unconditional data samples, serving as a reference for the overall distribution. In contrast, μ_c represents the mean of samples matching condition c (e.g., class label or prompt), capturing the conditional distribution shift.

Closed-form expression at $t \rightarrow 1$. At $t = 1$, the interpolated variable x_t equals the noise sample x_1 , i.e., $x_t = x_1$. In this case, the unconditional and conditional velocity predictions reduce to expectations:

$$\begin{aligned} v_u(x_1) &= \mathbb{E}[x_1 - x_0 | x_1] = x_1 - \mu_u \\ v_c(x_1, c) &= \mathbb{E}[x_1 - x_0 | x_1, c] = x_1 - \mu_c \end{aligned} \quad (4)$$

Substituting these expressions into the definition of the velocity gap $\delta(x_1, c) = v_c(x_1, c) - v_u(x_1)$, we obtain $\delta(x_1, c) = \mu_c - \mu_u$. Thus, the RATIO at $t = 1$ can be written explicitly as:

$$\text{RATIO}_{t=1}(c) = \frac{\|\delta(x_1, c)\|_2}{\|v_u(x_1)\|_2} = \frac{\|\mu_c - \mu_u\|_2}{\|x_1 - \mu_u\|_2}. \quad (5)$$

Equation (5) shows that the numerator depends only on how much the condition c shifts the data mean, while the denominator is mainly determined by the distance from the noise sample x_1 to the data mean. As a result, the initial RATIO is governed almost entirely by $\|\mu_c - \mu_u\|_2$, which can easily reach $\mathcal{O}(1)$ in typical cases.

Empirical validation. On ImageNet and MS-COCO, we observe consistently high initial RATIO values after SD3.5 VAE encoding (Figure 4a), confirming this as a dataset-level property rather than model-dependent.

We further trained RF-Transformer baselines on CIFAR-10 to test whether Equation (5) holds in practice. The measured $\text{RATIO}_{t=1}$ closely matches the pre-computed ideal RATIO (see Figure 3), with a strong linear correlation ($r = 0.92$). All values remain within $\mathcal{O}(1)$, confirming that a large yet bounded RATIO arises from dataset-level structure rather than model-specific factors.

3.3 OVERSIZED RATIO CAUSES SAMPLING COLLAPSE

This subsection presents two points: (1) A large $w\rho_{\max}$ exponentially amplifies sampling errors, as shown by a theoretical lower bound on trajectory divergence; (2) Experiments on Stable Diffusion v3.5 confirm that high initial RATIO degrades output quality. This supports the importance of RATIO-aware adaptive guidance.

3.3.1 LOWER BOUND OF SAMPLING ERRORS

Differential inequality for two trajectories. Fix a guidance scale $w > 1$ and consider the guided drift

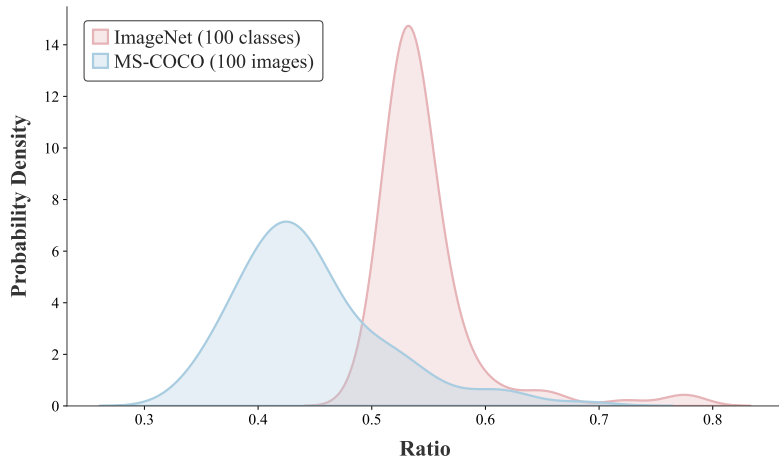
$$v_w(z) := v_u(z) + w\delta(z, c), \quad \delta(z, c) := v_c(z, c) - v_u(z), \quad (6)$$

where v_u is L_u -Lipschitz and $\|\delta(z, c)\|_2 \leq \rho_{\max}\|v_u(z)\|_2$ for all $z \in \mathbb{R}^d$. Let $x(t)$ and $y(t)$ be two solutions of $\dot{z} = v_w(z)$ on the interval $t \in [0, 1]$ with initial states $x(1) = x_1$ and $y(1) = y_1$.

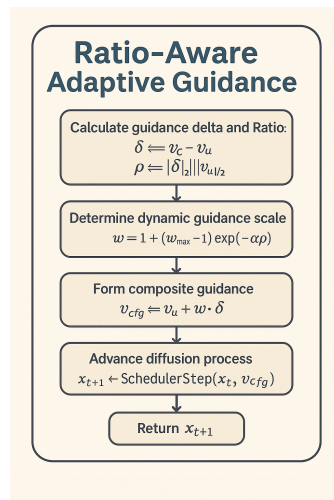
Distance between trajectories. Define the instantaneous Euclidean separation

$$\Delta(t) := \|x(t) - y(t)\|_2, \quad t \in [0, 1]. \quad (7)$$

This quantity measures how initial discrepancies propagate during guided sampling. The lower bound of $\Delta(t)$ can be established as follows (see Appendix A.2 for the complete derivation):

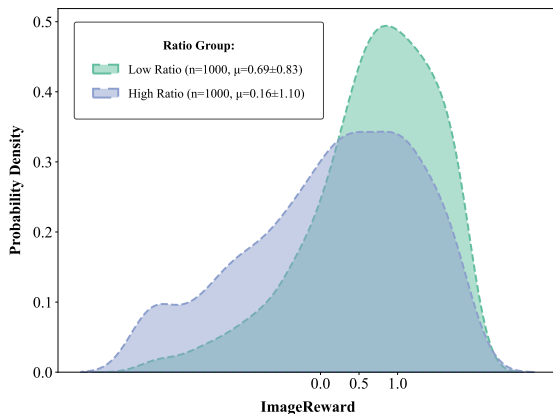


(a) Distribution of initial RATIO across ImageNet and MS-COCO.

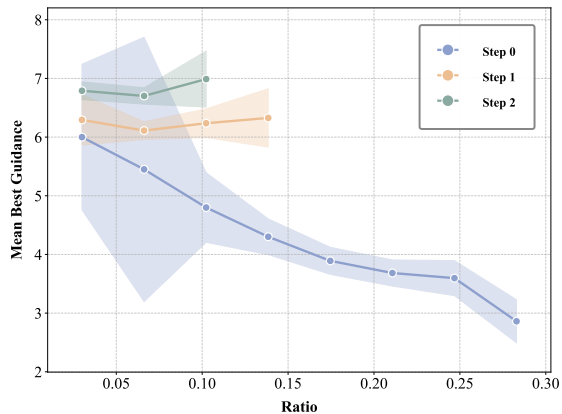


(b) Visualization of our method.

Figure 4: (a) Probability density distribution of the first-step conditional-unconditional RATIO ρ for each of the 100 ImageNet100 classes and 100 MS-COCO images. The majority of classes exhibit an initial RATIO concentrated around 0.5, indicating a relatively strong conditional signal at the very first sampling step. (b) A compact visualization of RAAG’s adaptive guidance scale scheduling based on step-wise RATIOS.



(a) Probability density distribution of low and high RATIO groups, respectively.



(b) Quantitative relationship between ρ_k and greedy-optimal guidance scales w_k^* in a 3-step search.

Figure 5: (a) Probability density of ImageReward scores across different RATIO groups. KDE plots of ImageReward for low-RATIO versus high-RATIO samples collected at the first reverse step. (b) Quantitative relationship between ρ_k and greedy-optimal guidance scales w_k^* in a 3-step search. For each reverse step $k < 3$, we plot the measured ρ_k against its corresponding w_k^* found by greedy tuning. The overall trend closely follows an exponential decay, demonstrating that the optimal guidance schedule across the first few steps can be unified under a single RATIO-based framework.

$$\Delta(t) \gtrsim \left(\Delta(0) - \frac{\lambda \|v_w(0)\|}{L_w} t \right) \exp \left[\frac{\lambda \sigma}{w(L_u + L_\delta)} |1 - w\rho| t \right]. \quad (8)$$

Role of $w\rho_{\max}$. Since Equation (8) contains the *common exponential factor* $\exp[\frac{\lambda\sigma}{L_u+L_\delta}|\frac{w\rho-1}{w}|t]$, the amplification of an *initial error* $\Delta(1)$ grows like $\exp[\frac{\lambda\sigma}{L_u+L_\delta}|\frac{w\rho-1}{w}|t]$, enlarging the lower bound of error.

As a result, whenever the product $w\rho_{\max}$ is large—whether because the guidance scale w is set aggressively or because the RATIO $\rho(x, c)$ is itself high—the reverse flow exhibits exponential sensitivity to any small perturbation (floating-point error, stochastic noise, random-seed variation, or modelling mismatch between δ and v_u). To validate its practical relevance, we supplement our theoretical analysis with targeted experiments: by grouping samples based on their first-step RATIO and comparing ImageReward scores, we show that lower values of RATIO markedly reduce error amplification and yield more stable, higher-quality generations.

3.3.2 EMPIRICAL VALIDATION

SD3.5 validation. We conducted controlled single-phase experiments on SD3.5 using 100 MS-COCO prompts (20 seeds per prompt, $w = 7.0$, 10 steps). Measuring $\rho(x_t, c)$ at the first reverse step, we grouped seeds by RATIO: the top/bottom 10 formed high/low-RATIO groups. ImageReward scores showed significantly higher performance for low-RATIO groups (0.69 ± 0.83 vs 0.16 ± 1.10 , $p < 0.0005$), as seen in Figure 5a.

3.4 RATIO-AWARE ADAPTIVE GUIDANCE

Greedy N -step search. We tune guidance scales only for the first N steps (later steps use default $w = 7.0$). Algorithm 1 details our greedy search that evaluates $17N$ guidance scale candidates per prompt via a 10-step sampling. This searching strategy includes the following key properties:

- Candidate sets always include current values, ensuring non-decreasing quality
- Monotonic improvement guarantees stable convergence to local optima

For each step $k < N$, we record $\rho_k = \text{RATIO}(x_{t_k}, c)$ and optimal scales w_k^* . Aggregating 1,000 prompts reveals the ρ_k - w_k^* functional trend, as shown in Figure 5b.

Exponential fit. Empirically, we observe that w_k^* exhibits an **exponential decay** with respect to ρ

$$w(\rho) = 1 + (w_{\max} - 1) \exp(-\alpha\rho), \quad \rho = \text{RATIO}(x_t, c). \quad (9)$$

Interpretation. The ceiling w_{\max} safeguards stability by enforcing grid bounds when $\rho \approx 0$, while the decay rate α governs guidance attenuation speed.

The resulting schedule is RATIO-aware, large enough to leverage a weak conditional signal, yet automatically damped when the RATIO spike makes guidance dangerous.

4 EXPERIMENTS

In this section, we conduct comprehensive experiments to evaluate the effectiveness, generalizability, and efficiency of RAAG across both image and video generation domains.

4.1 ACCELERATION ON TEXT-TO-IMAGE GENERATION

We first validate the effectiveness of RAAG in text-to-image tasks. Specifically, to further demonstrate the generality of our approach, we apply RAAG to leading text-to-image diffusion models including Stable Diffusion v3.5 (SD3.5) and Lumina-Next. We assess generation quality using common metrics such as ImageReward and CLIPScore, comparing our method against the corresponding baselines. Experimental results in Figure 6 show that RAAG consistently improves generation quality and semantic alignment.

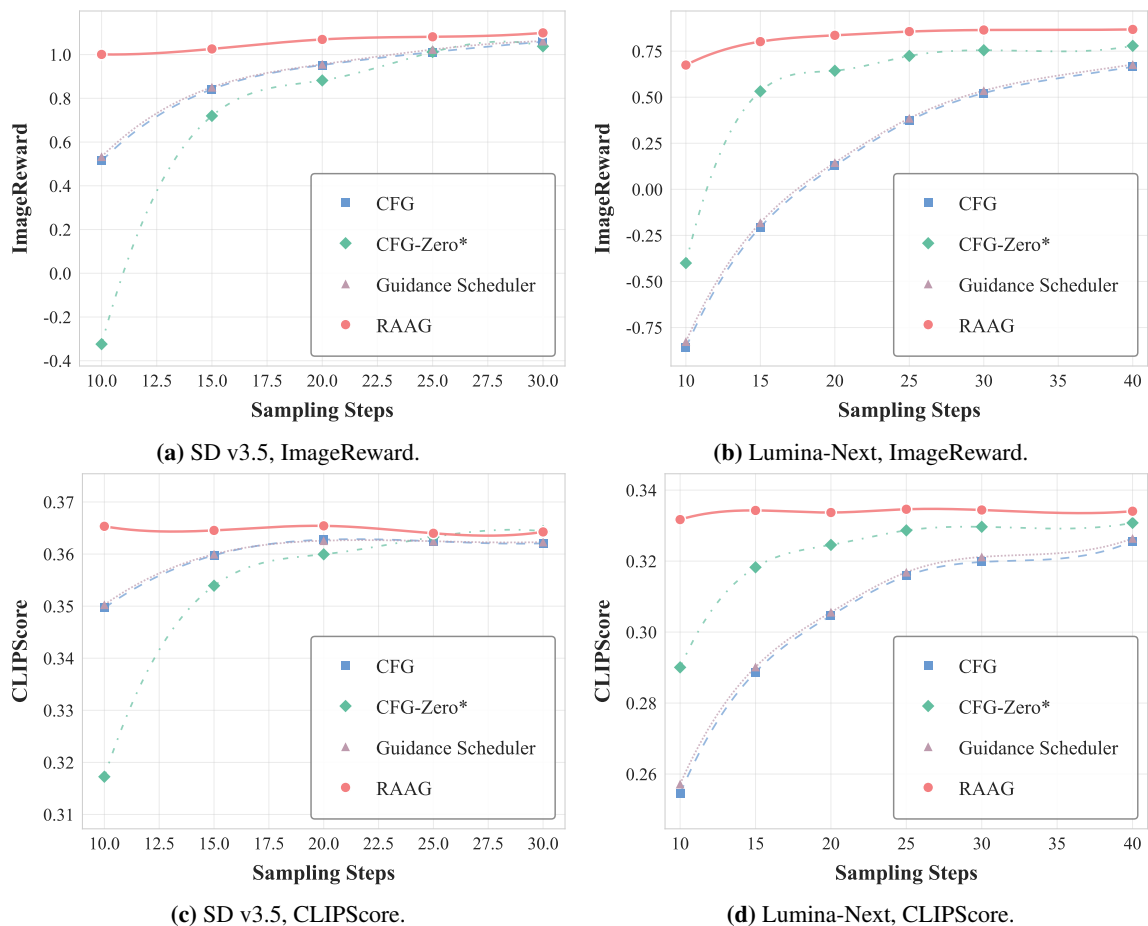


Figure 6: Quantitative results of comparative analysis with other baselines in text-to-image generation measured by ImageReward and CLIPScore. The results demonstrate RAAG’s remarkable superiority over others in low-step generation, achieving the quality of 30-step generation of CFG in only 10 steps.

4.2 ACCELERATION ON TEXT-TO-VIDEO GENERATION

We apply our RATIO-aware adaptive guidance to recent video diffusion frameworks and measure the quality of generated videos using standard metrics including Imaging Quality and Aesthetic Quality in vBench. Results in Figure 7 demonstrate that our method significantly enhances both the visual coherence and semantic consistency of generated videos compared to baseline methods.

4.3 ABLATION STUDIES AND PARAMETER SENSITIVITY

We conduct comprehensive ablation studies to justify our design choices and parameter selections as follows:

1. **Guidance Modeling Function:** We compare our exponential decay formulation against linear, piecewise-constant, and sigmoid functions to verify its suitability and performance advantages.

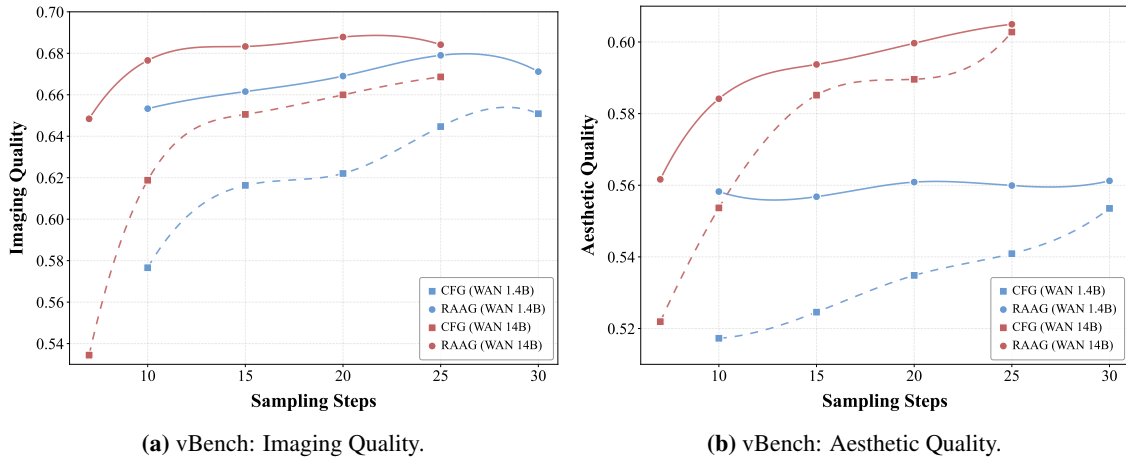


Figure 7: Quantitative results of text-to-video generation, comparing **CFG** and **RAAG** under vBench. The results strongly validate the effectiveness of RAAG on video generations, even overtaking CFG-WAN 14B just on WAN 1.4B.

- Hyperparameter Sensitivity:** We systematically analyze the impact of hyperparameters including the maximum guidance scale (w_{\max}) and the exponential decay rate (α). Sensitivity analysis reveals that RAAG maintains robust performance across reasonable parameter ranges, highlighting its practical utility.
- Scheduler Generalization:** We extend RAAG to the UniPC scheduler to validate its robustness across different schedulers. Figure 10 demonstrates consistent performance improvements of RAAG on UniPC, confirming its broad applicability.

Detailed quantitative and qualitative results of these ablations can be found in Appendix A.

5 CONCLUSION

We present RAAG, a plug-and-play guidance schedule rooted in our analysis of the critical RATIO-spike phenomenon. Without retraining or architectural changes, RAAG reliably outperforms existing methods—especially in low-step regimes—across diverse flow-based models, all with minimal computational overhead.

Limitations. Despite significant gains, RAAG faces two core constraints:

- Limited to Rectified Flow:** While RAAG demonstrates significant improvements on RF-based pipelines, it does not yield consistent benefits on diffusion-based architectures. This discrepancy may stem from differences in noise distributions, prediction targets, and model architectures. Developing a more general approach that is compatible with both paradigms is an important direction for future work.
- Limited Gains in High-Step Regimes:** While RAAG delivers significant improvements in low-step generation, its performance gains diminish substantially in high-step regimes, especially more than 40 steps. We attribute this limitation to the dominance of later-stage dynamics in extended trajectories: the decaying influence of initial RATIO reduces optimization leverage, while inherent model correction capabilities progressively compensate for earlier suboptimal conditions.

REFERENCES

- Angela Castillo, Jonas Kohler, Juan C Pérez, Juan Pablo Pérez, Albert Pumarola, Bernard Ghanem, Pablo Arbeláez, and Ali Thabet. Adaptive guidance: Training-free acceleration of conditional diffusion models. In *Proceedings of the AAAI Conference on Artificial Intelligence*, volume 39, pages 1962–1970, 2025.
- Hyungjin Chung, Jeongsol Kim, Geon Yeong Park, Hyelin Nam, and Jong Chul Ye. Cfg++: Manifold-constrained classifier free guidance for diffusion models. *arXiv preprint arXiv:2406.08070*, 2024.
- Prafulla Dhariwal and Alexander Nichol. Diffusion models beat gans on image synthesis. In *NeurIPS*, 2021.
- Patrick Esser, Sumith Kulal, Andreas Blattmann, Rahim Entezari, Jonas Müller, Harry Saini, Yam Levi, Dominik Lorenz, Axel Sauer, Frederic Boesel, Dustin Podell, Tim Dockhorn, Zion English, Kyle Lacey, Alex Goodwin, Yannik Marek, and Robin Rombach. Scaling rectified flow transformers for high-resolution image synthesis, 2024. URL <https://arxiv.org/abs/2403.03206>.
- Weichen Fan, Chenyang Si, Junhao Song, Zhenyu Yang, Yinan He, Long Zhuo, Ziqi Huang, Ziyue Dong, Jingwen He, Dongwei Pan, et al. Vchitect-2.0: Parallel transformer for scaling up video diffusion models. *arXiv preprint arXiv:2501.08453*, 2025a.
- Weichen Fan, Amber Yijia Zheng, Raymond A Yeh, and Ziwei Liu. Cfg-zero*: Improved classifier-free guidance for flow matching models. *arXiv preprint arXiv:2503.18886*, 2025b.
- Peng Gao, Le Zhuo, Dongyang Liu, Ruoyi Du, Xu Luo, Longtian Qiu, Yuhang Zhang, Chen Lin, Rongjie Huang, Shijie Geng, et al. Lumina-t2x: Transforming text into any modality, resolution, and duration via flow-based large diffusion transformers. *arXiv preprint arXiv:2405.05945*, 2024.
- Jonathan Ho and Tim Salimans. Classifier-free diffusion guidance. *arXiv preprint arXiv:2207.12598*, 2022.
- Peng Huang, Xue Gao, Lihong Huang, Jing Jiao, Xiaokang Li, Yuanyuan Wang, and Yi Guo. Chest-diffusion: A light-weight text-to-image model for report-to-cxr generation. *IEEE*, 2024.
- Tuomas Kynkäänniemi, Miika Aittala, Tero Karras, Samuli Laine, Timo Aila, and Jaakko Lehtinen. Applying guidance in a limited interval improves sample and distribution quality in diffusion models. *arXiv preprint arXiv:2404.07724*, 2024.
- Youwei Liang, Junfeng He, Gang Li, Peizhao Li, Arseniy Klimovskiy, Nicholas Carolan, Jiao Sun, Jordi Pont-Tuset, Sarah Young, Feng Yang, et al. Rich human feedback for text-to-image generation. In *CVPR*, 2024.
- Yaron Lipman, Ricky TQ Chen, Heli Ben-Hamu, Maximilian Nickel, and Matt Le. Flow matching for generative modeling. *arXiv preprint arXiv:2210.02747*, 2022.
- Xingchao Liu, Chengyue Gong, and Qiang Liu. Flow straight and fast: Learning to generate and transfer data with rectified flow. *arXiv preprint arXiv:2209.03003*, 2022.
- Haokai Ma, Yimeng Yang, Lei Meng, Ruobing Xie, and Xiangxu Meng. Multimodal conditioned diffusion model for recommendation. In *Companion Proceedings of the ACM Web Conference 2024*, pages 1733–1740, 2024.
- Dawid Malarz, Artur Kasymov, Maciej Zięba, Jacek Tabor, and Przemysław Spurek. Classifier-free guidance with adaptive scaling. *arXiv preprint arXiv:2502.10574*, 2025.
- Gustav Müller-Franzes, Jan Moritz Niehues, Firas Khader, Soroosh Tayebi Arasteh, Christoph Haarbuerger, Christiane Kuhl, Tianci Wang, Tianyu Han, Teresa Nolte, Sven Nebelung, et al. A multimodal comparison of latent denoising diffusion probabilistic models and generative adversarial networks for medical image synthesis. *Scientific Reports*, 13 (1):12098, 2023.
- Moritz Reuss, Ömer Erdiñç Yağmurlu, Fabian Wenzel, and Rudolf Lioutikov. Multimodal diffusion transformer: Learning versatile behavior from multimodal goals. *arXiv preprint arXiv:2407.05996*, 2024.

-
- Seyedmorteza Sadat, Otmar Hilliges, and Romann M Weber. Eliminating oversaturation and artifacts of high guidance scales in diffusion models. In *The Thirteenth International Conference on Learning Representations*, 2024.
- Ahmad Süleyman and Göksel Biricik. Grounding text-to-image diffusion models for controlled high-quality image generation. *arXiv preprint arXiv:2501.09194*, 2025.
- Wan Team. Wan: Open and advanced large-scale video generative models. 2025.
- Xi Wang, Nicolas Dufour, Nefeli Andreou, Marie-Paule Cani, Victoria Fernández Abrevaya, David Picard, and Vicky Kalogeiton. Analysis of classifier-free guidance weight schedulers. *arXiv preprint arXiv:2404.13040*, 2024.
- WANG Xi, Nicolas Dufour, Nefeli Andreou, CANI Marie-Paule, Victoria Fernandez Abrevaya, David Picard, and Vicky Kalogeiton. Analysis of classifier-free guidance weight schedulers. *Transactions on Machine Learning Research*.
- Mengfei Xia, Nan Xue, Yujun Shen, Ran Yi, Tieliang Gong, and Yong-Jin Liu. Rectified diffusion guidance for conditional generation. In *Proceedings of the Computer Vision and Pattern Recognition Conference*, pages 13371–13380, 2025.
- Changming Xiao, Qi Yang, Feng Zhou, and Changshui Zhang. From text to mask: Localizing entities using the attention of text-to-image diffusion models. *Neurocomputing*, 2024.
- Haotian Ye, Haowei Lin, Jiaqi Han, Minkai Xu, Sheng Liu, Yitao Liang, Jianzhu Ma, James Y Zou, and Stefano Ermon. Tfg: Unified training-free guidance for diffusion models. *Advances in Neural Information Processing Systems*, 37: 22370–22417, 2024.

A DERIVATION

A.1 APPROXIMATE LOWER BOUND OF THE TRAJECTORY DIFFERENCE

Assume $\Delta(t_0)$ is sufficiently small and positive. Shift time so that $t = t - t_0$ and $t_0 = 0$, hence $t \rightarrow 0$ and $z(t) \rightarrow z(0)$. Near $t = 0$ the dynamics are linearised by

$$\dot{z}(t) \approx J_{v_w} z(t), \quad (10)$$

where $J_{v_w} = J_{v_w}(y)$ is the Jacobian of v_w at y . With $\Delta(t) = \|z(t)\|$ and $u(t) = z(t)/\Delta(t)$,

$$\dot{\Delta}(t) \approx \Delta(t) u(t)^\top J_{v_w} u(t). \quad (11)$$

Jordan solution. Let J be the Jordan form of J_{v_w} with eigenvalues $\lambda_1, \dots, \lambda_m$ (blocks s_{ij} , multiplicities r_i). The solution of Equation (10) is

$$z(t) = \sum_{i=1}^m e^{\lambda_i t} \sum_{j=1}^{r_i} \sum_{k=1}^{s_{ij}} t^{k-1} c_{ijk} e_{ijk}. \quad (12)$$

In reality, the disturbance is random and possibly occur in any direction. To analyze stability, the focus is primarily on the worst-case scenario. Hence, for the sake of analysis, we suppose $z(0)$ lies in the direction of an eigenvector of the matrix J_{v_w} corresponding to a positive eigenvalue λ , i.e.,

$$J_{v_w} z(t) = \lambda z(t),$$

where $\lambda > 0$. Assume that $\delta(\cdot)$ is L_δ -Lipschitz and $v_w(\cdot)$ is L_w -Lipschitz where $L_w = L_u + wL_\delta$ and $L_\delta, L_w > 0$. Then

$$\begin{aligned} \dot{\Delta}(t) &\gtrsim \Delta(t) u(t)^\top \lambda u(t) \\ &= \lambda \Delta(t) \\ &= \lambda \|z(t) - 0\| \\ &\geq \frac{\lambda}{L_w} \|v_w(z(t)) - v_w(0)\| \\ &\geq \frac{\lambda}{L_w} (\|v_w(z(t))\| - \|v_w(0)\|) \\ &= \frac{\lambda}{L_u + wL_\delta} (\|v_u(z(t)) + w\delta(z(t))\| - \|v_w(0)\|) \\ &= \frac{\lambda}{L_u + wL_\delta} (\|v_u(z)\| \left\| \frac{v_u(z)}{\|v_u(z)\|} + w\rho \frac{\delta(z)}{\|\delta(z)\|} \right\| - \|v_w(0)\|). \end{aligned} \quad (13)$$

Let $v := \frac{v_u(z)}{\|v_u(z)\|}$ and $\delta := \frac{\delta(z)}{\|\delta(z)\|}$. Then

$$\begin{aligned} \left\| \frac{v_u(z)}{\|v_u(z)\|} + w\rho \frac{\delta(z)}{\|\delta(z)\|} \right\| &= \|v + w\rho\delta\| \\ &= \sqrt{(v + w\rho\delta)^\top (v + w\rho\delta)} \\ &= \sqrt{\|v\|^2 + w^2\rho^2\|\delta\|^2 + 2w\rho\delta^\top v} \\ &\geq \sqrt{(1 - w\rho)^2} \\ &= |1 - w\rho| \end{aligned} \quad (14)$$

Due to $w \geq 1$, we have

$$L_u + wL_\delta \leq w(L_u + L_\delta).$$

Then

$$\begin{aligned} \dot{\Delta}(t) &\gtrsim \lambda \|v_u(z)\| \frac{|1-w\rho|}{w(L_u+L_\delta)} - \lambda \frac{\|v_w(0)\|}{L_w} \\ &\gtrsim \lambda \sigma \frac{|1-w\rho|}{w(L_u+L_\delta)} \Delta(t) - \lambda \frac{\|v_w(0)\|}{L_w}, \end{aligned} \quad (15)$$

where $J_{v_u} := J_{v_u}(y)$ is the Jacobian matrix of v_u and σ is the minimum singular value of J_{v_u} satisfying $\|v_u(z)\| \geq \sigma \Delta(t)$. Note that here we do not consider the trivial case $z(t)$ is in the kernel space of J_{v_u} .

Giving

$$\dot{\Delta}(t) \gtrsim A \Delta(t) - B, \quad A := \frac{\lambda \sigma}{w(L_u + L_\delta)} |1 - w\rho|, \quad B := \frac{\lambda}{L_w} \|v_w(0)\|. \quad (16)$$

Integral form (Newton-Leibniz). By applying the Newton-Leibniz formula to Equation (16), we derive the integral form:

$$\Delta(t) - \Delta(0) \gtrsim \int_0^t A \Delta(s) ds - Bt. \quad (17)$$

Integration (Grönwall). Applying the Grönwall inequality to Equation (17) yields:

$$\Delta(t) \gtrsim \Delta(0) - Bt + \int_0^t (\Delta(0) - Bs) A e^{A(t-s)} ds. \quad (18)$$

Bounding the right-hand side. Given $B \geq 0$ and $0 \leq s \leq t$, we relax the right-hand side of Equation (18) as follows:

$$\begin{aligned} \Delta(t) &\gtrsim \Delta(0) - Bt + \int_0^t (\Delta(0) - Bs) A e^{A(t-s)} ds \\ &\geq \Delta(0) - Bt + \int_0^t (\Delta(0) - Bt) A e^{A(t-s)} ds \\ &= (\Delta(0) - Bt) \left(1 + \int_0^t A e^{A(t-s)} ds\right). \end{aligned} \quad (19)$$

Differential identity and evaluation. Using the identity $d(-e^{A(t-s)}) = A e^{A(t-s)} ds$, we simplify:

$$\begin{aligned} \Delta(t) &\gtrsim (\Delta(0) - Bt) \left(1 + \int_0^t A e^{A(t-s)} ds\right) \\ &= (\Delta(0) - Bt) \left(1 + \int_0^t d[-e^{A(t-s)}]\right) \\ &= (\Delta(0) - Bt) \left(1 + [-e^{A(t-s)}] \Big|_0^t\right) \\ &= (\Delta(0) - Bt) e^{At}, \end{aligned} \quad (20)$$

where A, B are defined in Equation (16).

Sensitivity condition. As $t \rightarrow 0$, the first-order approximation yields $\Delta(0) - Bt \approx \Delta(0) \geq 0$, as established in Equation (20). Therefore, we only need to consider the minimum of the amplification coefficient $A = \frac{\lambda\sigma}{w(L_u + L_\delta)} |1 - w\rho|$, which is minimized when $|1 - w\rho| \approx 0$, i.e.

$$w \approx \frac{1}{\rho} \quad (\rho = \|\delta(z)\|/\|v_u(z)\|),$$

which suppresses exponential growth and limits the sensitivity of $\Delta(t)$ to perturbations.

A.2 UPPER BOUND OF THE TRAJECTORY DIFFERENCE.

The following derivation details the process of obtaining the upper bound of the trajectory difference:

Time derivative of $\Delta(t)$. Let $z(t) := x(t) - y(t)$ and define the separation $\Delta(t) := \|z(t)\|_2$. Using the chain rule for the Euclidean norm,

$$\frac{d}{dt}\Delta(t) = \frac{z(t)^\top}{\|z(t)\|_2} \frac{d}{dt}z(t) = \frac{z(t)}{\Delta(t)} \cdot [v_w(x(t)) - v_w(y(t))]. \quad (21)$$

Introduce the unit vector $u(t) := z(t)/\Delta(t)$, so that $\|u(t)\|_2 = 1$. Equation (21) becomes

$$\frac{d}{dt}\Delta(t) = u(t)^\top [v_w(x(t)) - v_w(y(t))]. \quad (22)$$

For Equation (22), applying the Cauchy–Schwarz inequality $|a^\top b| \leq \|a\|_2 \|b\|_2$ with $a = u(t)$ and $b = v_w(x(t)) - v_w(y(t))$ gives

$$\left| \frac{d}{dt}\Delta(t) \right| \leq \|v_w(x(t)) - v_w(y(t))\|_2. \quad (23)$$

Because $\Delta(t) \geq 0$, the left-hand side of Equation (23) is non-negative, so the absolute value can be dropped to yield the upper bound used later:

$$\frac{d}{dt}\Delta(t) \leq \|v_w(x(t)) - v_w(y(t))\|_2. \quad (24)$$

Bounding the velocity difference. For arbitrary $x, y \in \mathbb{R}^d$,

$$\begin{aligned} \|v_w(x) - v_w(y)\|_2 &\leq \|v_u(x) - v_u(y)\|_2 + w\|\delta(x, c) - \delta(y, c)\|_2 \\ &\leq L_u\|x - y\|_2 + w[\|\delta(x, c)\|_2 + \|\delta(y, c)\|_2] \\ &\leq L_u\|x - y\|_2 + w\rho_{\max}[\|v_u(x)\|_2 + \|v_u(y)\|_2] \\ &\leq L_u\|x - y\|_2 + w\rho_{\max}[\|v_u(y)\|_2 + L_u\|x - y\|_2 + \|v_u(y)\|_2] \\ &= L_u(1 + w\rho_{\max})\|x - y\|_2 + 2w\rho_{\max}\|v_u(y)\|_2. \end{aligned} \quad (25)$$

The penultimate line uses the triangle inequality and the Lipschitz property $\|v_u(x)\|_2 \leq \|v_u(y)\|_2 + L_u\|x - y\|_2$.

Applying the bound to the trajectories. Substituting $x = x(t)$ and $y = y(t)$ in Equation (25) and combining with Equation (24) yields

$$\boxed{\frac{d}{dt}\Delta(t) \leq L_u(1 + w\rho_{\max})\Delta(t) + 2w\rho_{\max}\|v_u(y(t))\|_2.} \quad (26)$$

Grönwall preparation. Because $t \in [0, 1]$ is compact and v_u is continuous, by the Weierstrass Extreme Value Theorem the quantity

$$V_{\max} := \sup_{s \in [0, 1]} \|v_u(y(s))\|_2 \quad (27)$$

is finite. Replacing the last factor in Equation (26) with V_{\max} gives the linear Grönwall form

$$\boxed{\frac{d}{dt} \Delta(t) \leq L_u(1 + w\rho_{\max}) \Delta(t) + 2w\rho_{\max} V_{\max}.} \quad (28)$$

Consequences for generative quality. Solve the linear differential inequality Equation (28) by Grönwall’s lemma:

$$\Delta(t) \leq \left(2w\rho_{\max} V_{\max} t + \Delta(0)\right) e^{L_u(1+w\rho_{\max})t}. \quad (29)$$

The upper bound is intrinsically linked to the exponential term with regard to $w\rho$, further demonstrating the inherent instability of the sampling trajectory.

A.3 GREEDY N-STEP SEARCH ALGORITHM

We detail the implementation of the Greedy N-Step Search algorithm introduced in Section 3.4, as shown in Algorithm 1.

Algorithm 1 Greedy N -Step Search

Require: Default guidance scale $w = 7$, step count T , search depth N

Ensure: Optimized guidance scales $\{w_t^*\}_{t=0}^{N-1}$

1: **Initialization:**

2: Set $w_t \leftarrow 7$ for all steps $t \in \{0, \dots, T-1\}$

3: Define search grid $\mathcal{W} \leftarrow \{1, 1.5, 2, \dots, 9\}$ ▷ 0.5 spacing

4: **for** $t = 0$ **to** $N - 1$ **do**

5: **Step- t Search:**

6: Fix $\{w_0^*, \dots, w_{t-1}^*\}$ from previous steps

7: $w_t^* \leftarrow \arg \max_{w \in \mathcal{W}} \text{ImageReward}(w_0^*, \dots, w_{t-1}^*, w, 7, \dots, 7)$

8: **end for**

9: **Return** $(w_0^*, \dots, w_{N-1}^*)$ ▷ Steps N to $T - 1$ keep $w = 7$

B EXPERIMENTS

B.1 TEXT-TO-IMAGE GENERATION MEASURED BY GENEVAL

We further validate RAAG’s effectiveness using GenEval across multiple metrics. As shown in Table 1, RAAG consistently outperforms CFG in most scenarios.

B.2 PERFORMANCE ON DIFFUSION MODELS

In this section, we assess the applicability of RAAG to Stable Diffusion v2, examining its integration with score-based diffusion models. Preliminary results in [TODO] reveal subpar performance, highlighting limitations in our current approach. This discrepancy merits deeper investigation and will guide our future work.

Table 1: Quantitative results of text-to-image generation measured by GenEval. The evaluation demonstrates RAAG’s consistent superiority over standard CFG across different dimensions of GenEval, attaining a maximum **+21.25% absolute improvement** on the **Single Object** metric.

Model	Method	Single Object	Two Object	Overall Score
SD35	CFG	96.25%	85.00%	0.9063
SD35	RAAG	98.75%	85.00%	0.9188
Lumina-Next	CFG	71.25%	35.00%	0.5313
Lumina-Next	RAAG	92.50%	45.00%	0.6875

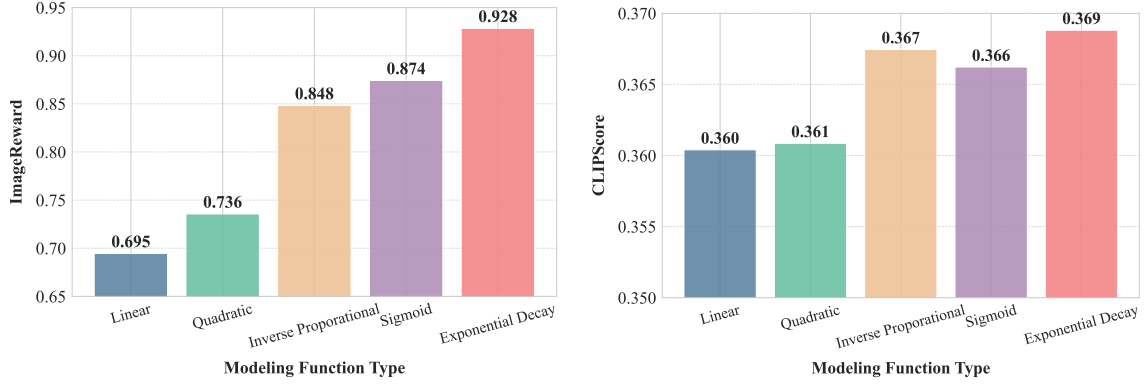
Table 2: Quantitative results of text-to image generation on Stable Diffusion v2, comparing RAAG and CFG. *Note:* decay rate $\alpha = 12$, guidance ceiling $w_{\max} = 18$.

Step	ImageReward		CLIPScore	
	RAAG	CFG	RAAG	CFG
10	-0.4306	-0.0983	0.3498	0.3578
20	-0.2368	0.0814	0.3575	0.3622
30	-0.1807	0.1463	0.3586	0.3635
40	-0.1444	0.1702	0.3575	0.3641

B.3 ABLATION STUDIES

In this section, we provide supplementary quantitative results from the ablation studies discussed in Section 4.3.

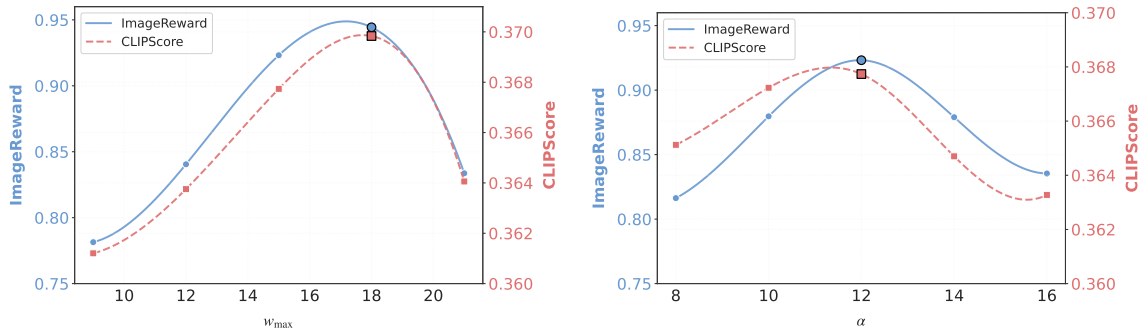
- Modeling Function Type (Figure 8):** We have conducted comparative analysis of modeling functions relating guidance scale to RATIO, demonstrating the superior performance of our selected formulation.
- Hyperparameter Sensitivity (Figure 9):** Through rigorous grid search over the parameter space, we verify RAAG’s insensitivity to hyperparameter selection, with performance variations remaining minor across all tested configurations.
- Scheduler Generalization (Figure 10):** We have conducted further extension of RAAG to UniPC to demonstrate consistent performance across different sampling schedulers, confirming architecture-agnostic applicability.



(a) Modeling function comparison: ImageReward.

(b) Modeling function comparison: CLIPScore.

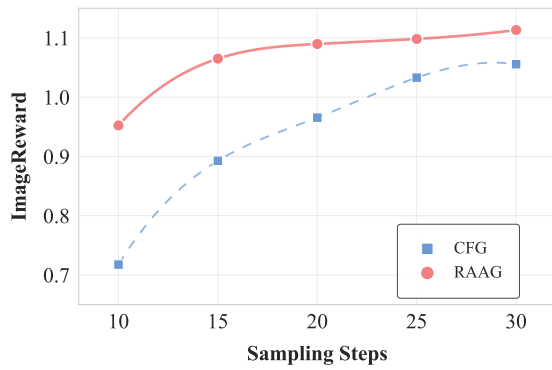
Figure 8: Ablation studies on different types of modeling functions. The comparative results demonstrate that the exponential decay function delivers the optimal fitting results among other functions, validating the soundness of our method.



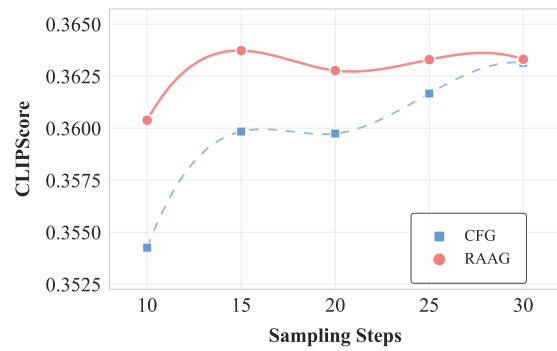
(a) Ablation studies on w_{\max} .

(b) Ablation studies on α .

Figure 9: Ablation studies on hyperparameters w_{\max} and α . Figures 9a and 9b present the variation trends of ImageReward and CLIPScore with respect to hyperparameters and validate our optimal selection of w_{\max} and α , indicating that the generation quality of RAAG is largely insensitive to hyperparameter selection, with performance sustained across an extensive parameter space.



(a) SD35 UniPC, ImageReward.



(b) SD35 UniPC, CLIPScore.

Figure 10: Ablation studies of schedulers on UniPC. The comparative results present the consistent superiority of RAAG over CFG across different schedulers, further validating the wide-ranging adaptability of our method.